Symmetry-engineered nodal lines and hourglass fermions in patterned two-dimensional electron gas

Bing Liu ●,[1,*] Zhao Liu,[2,3] Wenjun Zhang,[1] and Z. F. Wang[3,4,†]

[1]*School of Physics and Electronic Information, Weifang University, Weifang, Shandong 261061, China*
[2]*Department of Materials Science and Engineering, Monash University, Clayton, 3800 Victoria, Australia*
[3]*Hefei National Research Center for Physical Sciences at the Microscale, CAS Key Laboratory of Strongly-Coupled Quantum Matter Physics,*
Department of Physics, University of Science and Technology of China, Hefei, Anhui 230026, China
[4]*Hefei National Laboratory, University of Science and Technology of China, Hefei, Anhui 230088, China*

In most cases, the formation of topological quantum states requires intrinsic crystalline symmetry to protect either discrete or continuous degeneracies in real materials, which greatly hinders their realization in practice. Patterned two-dimensional electron gas (2DEG), on the other hand, has become a very effective external means to manipulate the symmetry to whatever we want. Here, taking nonsymmorphic symmetries as the focus of attention, based on patterned 2DEG decoration, we reveal rich band-crossing features in two-dimensional systems. It is demonstrated that in the presence of intrinsic spin-orbital coupling (SOC), wallpaper groups *p2mg*, *p2gg*, and *p4mg* possess fourfold-degenerate Dirac nodal lines, and if Rashba SOC is further considered, the fourfold-degenerate nodal lines disappear and hourglass Weyl fermions then emerge. Our results not only afford an attractive route for designing robust nodal-line and hourglass Weyl semimetals in reality, but also pave the way for designing ideal macroscale materials through rational extrinsic symmetry engineering.

I. INTRODUCTION

During the past decades, beginning with the discovery of topological insulators [1–5], topological materials have become the subject of great interest and widespread enthusiasm in condensed matter physics, in which topological semimetals are occupying an important position, including Dirac [6–11], Weyl [6,12–17], and nodal-line semimetals [7,18–25]. Distinct from Dirac and Weyl semimetals with isolated band-crossing points, the crossings form either a continuous line or a closed loop in momentum space near the Fermi energy in nodal-line semimetals. Like the discrete cousins, nodal-line semimetals are classified as Dirac and Weyl ones depending on the degree of degeneracy. Since the low-energy quasiparticles in nodal-line materials behave differently from conventional Schrödinger-type fermions, several novel properties have been proposed, such as chiral anomaly [26] and nearly flat drumheadlike surface states [27–29], which have opened an important route for achieving high-temperature superconductivity [30,31], unique Landau energy level [32,33], and anomaly in electromagnetic and transport response [34–36].

However, all these topological materials described above are based on intrinsic crystal symmetries, which are not flexible enough once the material is determined, such as specific crystal surface constraint, nonstable configuration. While recently, instead of only relying on the intrinsic sym-

metries, the possible use of external means to control the symmetry of a system has yet to be explored [37–40], in which patterned two-dimensional electron gas (2DEG) provides a very effective method, and has been widely studied both in theory and experiment [40–47]. Experimentally, the existing methods of implementing patterned 2DEGs can be classified into two types, quantum well (QW) etching and atom/molecule adsorption on a flat metal surface. The former is based on quantum wells where the external potential is achieved by first defining arrays of disks using e-beam nanolithography and then etching away the material outside the disks by inductive coupled reactive ion shallow etching [48,49]. In this method, the potential behaves as a weak negative value [50] and is determined by the etching depth. For the latter, external potential is introduced by absorbing atoms/molecules on a flat metal surface viewed as a 2DEG by the scanning tunneling microscopy tip [51,52], in which the potential value is dependent on different atoms/molecules absorbed (It is noted that the underlying 2DEG lattice may differ from the atom/molecule lattice [53]). Within this method, the absorbed atoms/molecules normally apply a repulsive potential to the metal surface states. A related experimental technique for an atom/molecule lattice is the self-assembly, where organic porous networks are used to confine the surface electrons [54,55], however, lattices with nonsymmorphic symmetry have not been reported yet. At last, there are another two experimental techniques in realizing a patterned 2DEG: atomic force microscope (AFM) lithography and lithographic top-down patterning. Taking advantage of AFM lithography, nanoscale conducting regions can be created in a $LaAlO_3/SrTiO_3$ heterostructure and erased using voltages applied by a conducting AFM probe [40,56]. As for the lithographic top-down patterning, it can be realized on a

---

*To whom correspondence should be addressed: liubing@wfu.edu.cn
†To whom correspondence should be addressed: zfwang15@ustc.edu.cn

heterostructure consisting of a 2D electride encapsulated in hexagonal boron nitride where the external potential is introduced by etching a periodic pattern of holes through the heterostructure by electron-beam lithography. Such a method is very mature in fabricating graphene [57,58]. Therefore, dramatically, with this method one can design a system with all symmetries required for desired topological states, completely free from material constraints.

On the other hand, compared to symmorphic symmetries, nonsymmorphic symmetries are playing a more crucial role in generating stable crossings [59–61] since they offer an extra crystalline symmetry to protect the degeneracy against intrinsic spin-orbit coupling (SOC), which is inevitable in real materials. Very recently, some nonsymmorphic symmetries protected exotic band crossings have also been proposed, such as hourglass dispersions [37,59,62,63], nodal chains [64,65], and Möbius insulators [66,67]. Moreover, 2D Dirac nodal-line semimetal phases have only been confirmed in very few real systems in experiment, such as Cu_2Si [68–70], and CuSe [71], while they are not robust when taking SOC into account. Therefore, there remains an intensive material search for robust Dirac nodal line at present.

Encouraged by the fact that various exotic topological quantum states, such as hourglass fermions [37,72], Möbius insulators [66,67], and fourfold-degenerate Dirac fermions [73] have been well studied in all four nonsymmorphic wallpaper groups $p1g1$, $p2mg$, $p2gg$, and $p4mg$ [66,67,73–79], in this work, combining patterned 2DEG model and nonsymmorphic symmetries, we construct three systems belonging to wallpaper groups $p2mg$, $p2gg$, and $p4mg$, respectively, and discover a series of rich topological states, including Dirac nodal line, Weyl nodal line, and hourglass Weyl fermion (as listed in Table I). Among the four nonsymmorphic wallpaper groups, group $p1g1$ can be largely thought as 1D system which is thus ignored in this work. Our results not only afford an attractive route for designing robust nodal line and hourglass Weyl semimetals in reality, but also pave a way for designing ideal macroscale materials through rational extrinsic symmetry.

The remainder of this article is organized as follows: Sec. II sets the full 2DEG tight-binding model and corresponding lattice configurations. Secs III and IV describe detailed symmetry analysis, band calculation results, and k · p approximation for the nontrivial band crossings in two constructed systems. Sec V shows the effect of parameters

on bandwidth, and finally Sec. VI concludes our work.

II. CONSTRUCTION OF MODELS AND LATTICES

In this section, we describe the full 2DEG model and our constructed lattices. The method of patterned 2DEG model is elucidated as follows: the Hamiltonian of the system is [80]

$$H(\mathbf{k}) = \sum_{\mathbf{G}} \frac{\hbar^2}{2m^*} |\mathbf{k} + \mathbf{G}|^2 a_{\mathbf{G}}^{\dagger} a_{\mathbf{G}} + \sum_{\mathbf{G},\mathbf{G'}} V(\mathbf{G} - \mathbf{G'}) a_{\mathbf{G'}}^{\dagger} a_{\mathbf{G}},$$
(1)

where m^* is the electron effective mass. For the lowest conduction band in diamond-type or zinc-blende-type semiconductor quantum wells, m^* varies between $0.02m_e$ and $0.17m_e$ (m_e is the free electron mass) [81]. Here we simply consider $m^* = 0.02m_e$ and $m^* = 0.04m_e$ in our calculation. $\mathbf{G}$ is the reciprocal lattice vector, and $a^{\dagger}$ and a are creation and annihilation operators, respectively. $V(\mathbf{G})$ are the Fourier components of the potential, and can be expressed as

$$V(\mathbf{G}) = \sum_i \frac{\pi d U_0 J_1\left(\frac{1}{2}|\mathbf{G}|d\right)}{A|\mathbf{G}|} \exp\left(-i\mathbf{G} \cdot \mathbf{X}_i\right),$$
(2)

where A is the area of the unit cell and $\mathbf{X}_i$ is the center of the ith disk in unit cell. Here, the disks represent the external potential wells introduced by QW etching or potential barriers introduced by adatoms, respectively. $J_1(x)$ is the first-order Bessel function. Therefore, the Hamiltonian in Eq. (1) can further be expressed in the matrix form

$$\begin{bmatrix} \frac{\hbar^2|\mathbf{k}+\mathbf{G}_1|^2}{2m^*} + V_0 & V_{1-2} & \cdots & V_{1-n} \\ V_{2-1} & \frac{\hbar^2|\mathbf{k}+\mathbf{G}_2|^2}{2m^*} + V_0 & \cdots & V_{2-n} \\ \vdots & \vdots & \ddots & \vdots \\ V_{n-1} & V_{n-2} & \cdots & \frac{\hbar^2|\mathbf{k}+\mathbf{G}_n|^2}{2m^*} + V_0 \end{bmatrix},$$
(3)

where $V_{i-j} = V(\mathbf{G}_i - \mathbf{G}_j)$ and V_0 is a constant.

Intrinsic SOC is incorporated via the gradient of the muffin-tin potential:

$$H_{SO} = \frac{e\lambda}{\hbar}\boldsymbol{\sigma} \cdot (\mathbf{p} \times \mathbf{E}) = -\frac{\lambda}{\hbar}\boldsymbol{\sigma} \cdot (\nabla V \times \mathbf{p}),$$
(4)

where $\boldsymbol{\sigma}$ is the Pauli matrix, $\mathbf{p}$ is momentum, λ is coupling constant and $\mathbf{E}$ is in-plane electric field. Thus, H_{SO} can also be written into matrix form

$$H_{SO}(\mathbf{k}) = -i\lambda\sigma_z \otimes \begin{bmatrix} 0 & V_{1-2}[\mathbf{G}_{1-2} \times (\mathbf{G}_2 + \mathbf{k})]_z & \cdots & V_{1-n}[\mathbf{G}_{1-n} \times (\mathbf{G}_n + \mathbf{k})]_z \\ V_{2-1}[\mathbf{G}_{2-1} \times (\mathbf{G}_1 + \mathbf{k})]_z & 0 & \cdots & V_{2-n}[\mathbf{G}_{2-n} \times (\mathbf{G}_n + \mathbf{k})]_z \\ \vdots & \vdots & \ddots & \vdots \\ V_{n-1}[\mathbf{G}_{n-1} \times (\mathbf{G}_1 + \mathbf{k})]_z & V_{n-2}[\mathbf{G}_{n-2} \times (\mathbf{G}_2 + \mathbf{k})]_z & \cdots & 0 \end{bmatrix},$$
(5)

where $\sigma_z = \boldsymbol{\sigma} \cdot \hat{z}$ and $\mathbf{G}_{i-j} = \mathbf{G}_i - \mathbf{G}_j$. Clearly, the above matrix is diagonal, indicating that the spin-up and spin-down are decoupled because H_{SO} depends only on σ_z.

Moreover, for a realistic patterned 2DEG system without inversion symmetry, a Rashba SOC having the following form:

$$H_{RA} = \frac{\alpha}{\hbar}(p_y\sigma_x - p_x\sigma_y),$$
(6)

where α is also a coupling constant, also would be introduced through an effective field in the system. But for systems where the inversion symmetry is slightly broken and the out-of-plane potential is weak, such a SOC can be ignored, which allows us to
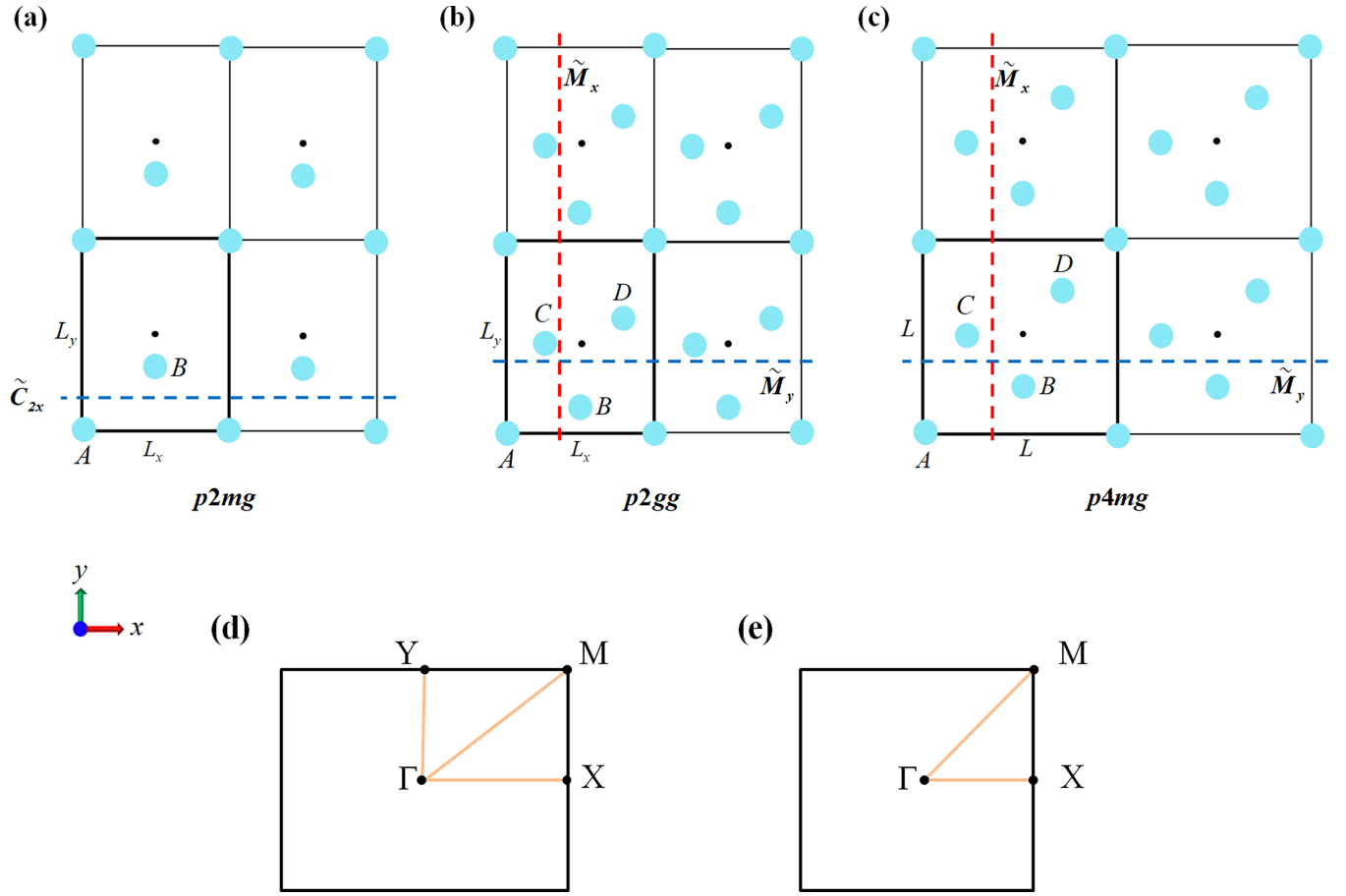
FIG. 1. (a)–(c) Schematic lattice structures for muffin-tin potential using nonsymmorphic symmetries of wallpaper groups *p2mg*, *p2gg* and *p4mg* with screw rotation $\tilde{C}_{2x}$ and glide mirror $\tilde{M}_x/\tilde{M}_y$ indicated with red and/or blue dashed lines. The black rectangle (square) represents the unit cell, L_x/L_y and L indicate the lattice parameters of the unit cell. The potential value is $U_0 > 0$ inside the light cyan disks and zero outside. (d) The BZ for Lattices1 and Lattice2 and (e) for Lattices3.

consider intrinsic SOC independently. The matrix form of H_{RA} is given by

$$H_{RA}(\mathbf{k}) = \alpha\sigma_x \otimes \begin{bmatrix} (\mathbf{G}_1 + \mathbf{k})_y & 0 & \dots & 0 \\ 0 & (\mathbf{G}_2 + \mathbf{k})_y & \dots & 0 \\ \vdots & \vdots & \ddots & \vdots \\ 0 & 0 & \dots & (\mathbf{G}_n + \mathbf{k})_y \end{bmatrix} - \alpha\sigma_y \otimes \begin{bmatrix} (\mathbf{G}_1 + \mathbf{k})_x & 0 & \dots & 0 \\ 0 & (\mathbf{G}_2 + \mathbf{k})_x & \dots & 0 \\ \vdots & \vdots & \ddots & \vdots \\ 0 & 0 & \dots & (\mathbf{G}_n + \mathbf{k})_x \end{bmatrix}. \quad (7)$$

Note that Eq. (7) locates at the antidiagonal direction of the whole Hamiltonian of order $2n$, while Eqs. (3) and (5) are at the diagonal direction, since H_{RA} is only the interaction between the same wave functions with inverse spin.

By taking all the above three terms into account, the total Hamiltonian is obtained:

$$H_{\text{total}}(\mathbf{k}) = H(\mathbf{k}) + H_{SO}(\mathbf{k}) + H_{RA}(\mathbf{k}). \quad (8)$$

As for the lattice, Figs. 1(a)–1(c) show the constructed lattice structures (labeled as Lattice1, Lattice2, and Lattice3) using muffin-tin potential in *p2mg*, *p2gg* and *p4mg*, respectively, where the potential value is $U_0 > 0$ (here, a positive U_0 value indicates a potential barrier and the values used in our calculation are either typical of values or in the same order of magnitude as those employed in confining 2DEGs [82])

inside the light cyan disks of diameter d and zero outside (the centers of the disks in the unit cell for three lattices are listed in Table II). The corresponding Brillouin zones (BZs) are shown in Figs. 1(d)–1(e). Due to the band structure results of Lattice2 and Lattice3 share very similar features, hence in the following discussions, we will just focus on the results for Lattice1 and Lattice2, and the results for Lattice3 are presented in Appendices A and B.

TABLE I. Degeneracy for different wallpaper groups with different types of SOC. Here AB means Dirac nodal line extending from A to B and A → B means that the Weyl point lies between A and B, A and B are two different high symmetric k points in the irreducible Brillouin zone (BZ).

wallpaper group	Intrinsic SOC	Intrinsic + Rashba SOC
$p2mg$	1 Dirac nodal line (XM)	2 hourglass Weyl fermions ($\Gamma \to X$, $Y \to M$)
$p2gg$	2 Dirac nodal lines (XM, YM)	2 hourglass Weyl fermions ($\Gamma \to X$, $\Gamma \to Y$)
$p4mg$	1 Dirac nodal line (XM)	1 hourglass Weyl fermion ($\Gamma \to X$)

III. LATTICE1

Having constructed the patterned 2DEG model, the next step for a desired study of topological state is to consider the above lattice one by one. The workflow for analysis in regard to Lattice1 is described in the subsequent sections, with three different methods: symmetry analysis, numerical calculation, and k · p approximation taken into account. A very similar analysis for Lattice2 is then given in the next section.

A. $\lambda \neq 0$, $\alpha = 0$: a Dirac nodal line

1. Symmetry analysis

In this section, we give a detailed symmetry analysis on possible nontrivial band crossings for Lattice1 when only intrinsic SOC is considered. We start with finding generators of the space group, then the little groups of some high-symmetry points/paths are determined to provide a detailed proof for consequential degeneracy.

When intrinsic SOC is present, the lattice structure of Lattice1 belongs to space group $Pmma$ (No. 51) and there are three generators: inversion P, twofold rotation C_{2z} and screw axis rotation $\{C_{2x}|\frac{1}{2}00\}$. By combining these three operations, we can obtain another two symmetries $M_x : (x, y, z) \to (-x + \frac{1}{2}, y, z)$ and $\tilde{M}_y : (x, y, z) \to (x + \frac{1}{2}, -y, z)$. Here the tilde denotes a nonsymmorphic operation, which involves a translation with fractional lattice parameters. In addition, no magnetic order is concerned in our systems, so time reversal symmetry T is preserved.

The X-M path is in the invariant subspace of M_z, so each Bloch state $|u\rangle$ on the path can be chosen as an eigenstate of M_z. We find that on X-M

$$M_z^2 = \overline{E} = -1, \tag{9}$$

where $\overline{E}$ denotes the 2π spin rotation and a 2π rotation on spin-1/2 fermion gives a -1. Hence the eigenvalue of M_z along this path is $g_z = \pm i$.

TABLE II. Center positions of the disks in Figs. 1(a)–1(c). The positions here are fractional coordinates, and δ, δ_1, $\delta_2 \in (0, \frac{1}{2})$.

Wallpaper group	A	B	C	D
$p2mg$	$(0, 0)$	$(\frac{1}{2}, \delta)$	\	\
$p2gg$	$(0, 0)$	$(\frac{1}{2}, \delta_1)$	$(\delta_2, \frac{1}{2})$	$(\frac{1}{2} + \delta_2, \frac{1}{2} + \delta_1)$
$p4mg$	$(0, 0)$	$(\frac{1}{2}, \delta)$	$(\delta, \frac{1}{2})$	$(\frac{1}{2} + \delta, \frac{1}{2} + \delta)$

We also note that each k point on X-M is invariant under the combined antiunitary operation $\tilde{M}_y T$. Since

$$(\tilde{M}_y T)^2 = e^{ik_x} = -1 \tag{10}$$

on X-M, therefore the bands along this path have a Kramer-like double degeneracy. The commutation relation between M_z and $\tilde{M}_y$ is

$$M_z \tilde{M}_y = \overline{E} \tilde{M}_y M_z \tag{11}$$

on X-M, i.e., anticommutation relation $\{M_z, \tilde{M}_y\} = 0$. Hence, for an eigenstate $|u\rangle$ with M_z eigenvalue g_z, we have

$$M_z(\tilde{M}_y T |u\rangle) = g_z(\tilde{M}_y T |u\rangle), \tag{12}$$

showing that the two Kramers partners $|u\rangle$ and $\tilde{M}_y T |u\rangle$ share the same eigenvalue g_z.

Additionally, X-M is also the invariant subspace of M_x. The commutation relation between M_z and M_x is

$$M_z M_x = \overline{E} M_x M_z, \tag{13}$$

i.e., anticommutation relation $\{M_z, M_x\} = 0$ on X-M, thus we have

$$M_z(M_x |u\rangle) = -g_z(M_x |u\rangle). \tag{14}$$

Indicate the existence of another degenerate eigenstate $M_x |u\rangle$, which has the opposite eigenvalue $-g_z$. Thus, totally, four degenerate orthogonal states $\{|u\rangle, \tilde{M}_y T |u\rangle, M_x |u\rangle, (\tilde{M}_y T)M_x |u\rangle\}$ form a degenerate quartet for each k point on X-M, implying that there is a Dirac nodal line along X-M when intrinsic SOC present, and it is completely protected by nonsymmorphic symmetries.

It is important to note that the above symmetry analysis is valid when only intrinsic SOC is present, in which inversion P is preserved. The conclusion is no longer valid if Rashba SOC also taken into account, as we discussed in Sec. III B 1.

2. Numerical result

We now perform band structure calculation in presence of intrinsic SOC for Lattice1. As shown in Fig. 2(a), we can observe several nontrivial band features: (i) Each band is at least twofold-degenerate due to the presence of both time reversal and inversion symmetry (with $(PT)^2 = -1$). (ii) Two groups of twofold degeneracy overlap at the M point which makes M point fourfold-degenerate. Moreover, M is not the only point with fourfold degeneracy. A visualized 3D band structure [Fig. 2(b)] shows that each point along X-M path is fourfold-degenerate as well, so the bands along X-M path actually form a fourfold-degenerate Dirac nodal line, consistent with previous symmetry analysis. In addition, it is clear that
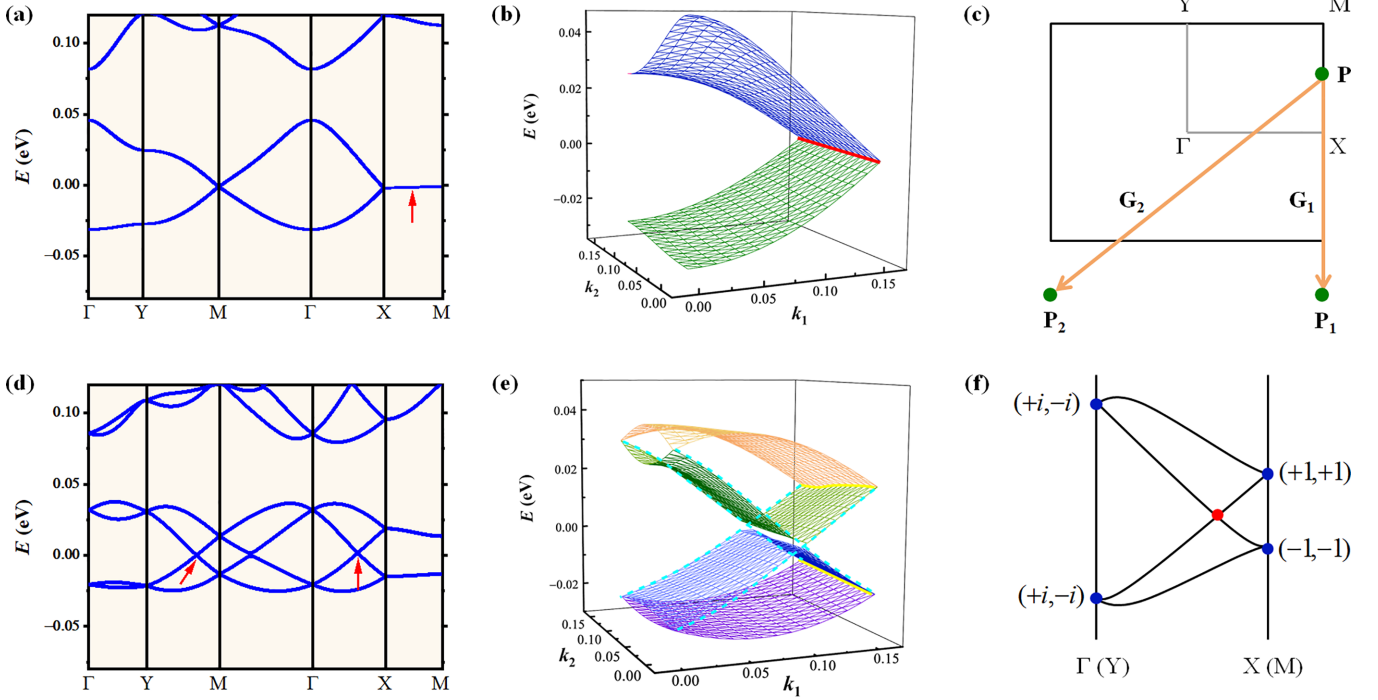
FIG. 2. Calculated band structures for the lowest four bands in presence of intrinsic SOC and Rashba SOC for Lattice1. Band structure along high-symmetry paths in (a) intrinsic SOC case and in (d) both intrinsic SOC and Rashba SOC case. The 3D plot in (b) shows a 1D Dirac nodal line, indicated by red solid line, along BZ boundary in intrinsic SOC case and that in (e) shows two hourglass-type dispersions and two Weyl nodal lines, indicated with cyan dashed lines and yellow solid lines, respectively, in both intrinsic SOC and Rashba SOC case. (c) Illustration of the translation for **P** on Dirac nodal line X-M to $\mathbf{P}_1$ and $\mathbf{P}_2$. (f) Schematic figure shows the hourglass dispersion along path Γ-X (Y-M), characterized by a hourglass cone with four degenerate points at boundary (blue dot) and one degenerate point at center (red dot). The numbers in the bracket denote the eigenvalue g_y at the degenerate point. In our calculation, $U_0 = 0.8$ eV, $L_x = 20$ nm, $L_y = 25$ nm, $m^* = 0.02m_e$, $d = 10$ nm, $\lambda = 3.2 \times 10^{-18}$ m², $\alpha = 3 \times 10^{-10}$ eV m. The degenerate point energy at M in (a) and between Y-M in (d) is set to zero, respectively.

the dispersion along X-M is quite flat for the parameters we used.

3. k · p approximation

At last, we present analytical solution for the energy dispersion relation of the Dirac nodal line in Lattice1 using degenerate perturbation theory. Specifically, we concentrate on the states with wave vector $\mathbf{q} + \mathbf{P}$ near arbitrary **P** point on path X-M, i.e., $\mathbf{q} << \mathbf{P}$, where $\mathbf{P} = (\pi/L_x, k_y)$, $k_y \in (-\pi/L_y, \pi/L_y)$ [see Fig. 2(c)]. The original wave function $\psi_{\mathbf{k}}(\mathbf{r})$ can be approximately expressed as a linear combination of two plane-wave states:

$$\psi_{\mathbf{k}}(\mathbf{r}) = \frac{1}{\sqrt{2A}}[c_1 e^{i(\mathbf{k}+\mathbf{G}_1)\cdot\mathbf{r}} + c_2 e^{i(\mathbf{k}+\mathbf{G}_2)\cdot\mathbf{r}}], \quad (15)$$

where A is the area of unit cell and $\mathbf{G}_1/\mathbf{G}_2$ represents reciprocal vector. Since we only concern the states near **P** point, let us substitute $\mathbf{k}$ for $\mathbf{q} + \mathbf{P}$, then $\psi_{\mathbf{k}}(\mathbf{r})$ can further be expressed as

$$\psi_{\mathbf{q}}(\mathbf{r}) = \frac{1}{\sqrt{2A}}[c_1 e^{i(\mathbf{q}+\mathbf{P}_1)\cdot\mathbf{r}} + c_2 e^{i(\mathbf{q}+\mathbf{P}_2)\cdot\mathbf{r}}]. \quad (16)$$

The reason for choosing the basis $(\mathbf{P}_1, \mathbf{P}_2)$ is that they are connected by the minimum reciprocal vector $\mathbf{G}_1/\mathbf{G}_2$ with **P**, and they have a same energy for pure 2DEG ($\mathbf{E}(\mathbf{k}) = \hbar^2\mathbf{k}^2/2m^*$).

Hence, we can express the eigenstate as a two-component column vector $\mathbf{c} = (c_1, c_2)^T$. Within this basis, the Hamiltonian in Eq. (3) can be written into

$$H(\mathbf{q}) = \begin{bmatrix} \frac{\hbar^2}{2m^*}(\mathbf{q}+\mathbf{P}_1)^2 + V_0 & V_{1-2} \\ V_{2-1} & \frac{\hbar^2}{2m^*}(\mathbf{q}+\mathbf{P}_2)^2 + V_0 \end{bmatrix}. \quad (17)$$

Here $V_0 = \frac{\pi d^2 U_0}{2A}$ is a constant. Further using Eq. (2) and Table II, we can obtain

$$V_{1-2} = V_{2-1}^* = \frac{\pi d U_0 J_1\left(\frac{1}{2}|\mathbf{G}_{1-2}|d\right)}{A|\mathbf{G}_{1-2}|}(e^{-i\cdot 0} + e^{-i\cdot\pi}) = 0, \quad (18)$$

then Hamiltonian Eq. (17) changes into

$$H(\mathbf{q}) = \begin{bmatrix} \frac{\hbar^2}{2m^*}(\mathbf{q}+\mathbf{P}_1)^2 + V_0 & 0 \\ 0 & \frac{\hbar^2}{2m^*}(\mathbf{q}+\mathbf{P}_2)^2 + V_0 \end{bmatrix}, \quad (19)$$

and H_{SO} equals zero. Clearly, the Hamiltonian is completely determined by the diagonal terms $\frac{\hbar^2}{2m^*}(\mathbf{q}+\mathbf{P}_1)^2 + V_0$ and $\frac{\hbar^2}{2m^*}(\mathbf{q}+\mathbf{P}_2)^2 + V_0$, so each crossing point on X-M is formed by an intersection between two different bands, meeting the condition of a Dirac state. In addition, the intrinsic SOC term has no effect on the energy, that is to say, it is a truly robust

Dirac nodal line. The dispersion relation of Eq. (19) is given

$$E(\mathbf{q}) = \frac{\hbar^2}{2m^*}\left\{\mathbf{q}^2 \pm \frac{2\pi}{L_x}q_x + 2\left(k_y - \frac{2\pi}{L_y}\right)q_y\right.$$

$$\left. + \frac{\pi^2}{L_x^2} + \left(k_y - \frac{2\pi}{L_y}\right)^2\right\} + \frac{\pi d^2 U_0}{2A}. \quad (20)$$

Obviously, the band dispersion around X-M is indeed linear and the group velocities remain constant.

B. $\lambda \neq 0$, $\alpha \neq 0$: two hourglass Weyl points

1. Symmetry analysis

In this section, we then give a detailed symmetry analysis on possible nontrivial band crossings when both intrinsic SOC and Rashba SOC are considered.

Once Rashba SOC is also involved, inversion P is destroyed and the original space group $Pmma$ (No. 51) is reduced to $Pma2$ (No. 28). Here corresponding generators are the following two symmetries: $M_x : (x, y, z) \rightarrow (-x + \frac{1}{2}, y, z)$ and $\tilde{M}_y : (x, y, z) \rightarrow (x + \frac{1}{2}, -y, z)$. In the following text, we show that there are two twofold-degenerate Weyl nodal lines and two hourglass Weyl points, both resulted from nonsymmorphic symmetries.

Firstly, let us consider the high-symmetry path X-M $(\pi/L_x, k_y, 0)$, where $-\pi/L_y < k_y \leqslant \pi/L_y$. The path lies on $k_x = \pi/L_x$ plane which is invariant under M_x, so each Bloch state $|u\rangle$ there can be chosen as an eigenstate of M_x. Due to

$$M_x^2 = \overline{E} = -1 \quad (21)$$

on X-M, hence the eigenvalue g_x of M_x must be $\pm i$.

Note that each k point on X-M is also invariant under the combined anti-unitary operation $\tilde{M}_y T$. Since

$$(\tilde{M}_y T)^2 = e^{ik_x} = -1 \quad (22)$$

on X-M, thus the bands along X-M will have a Kramer-like double degeneracy. Moreover, the commutation relation between M_x and $\tilde{M}_y$ is

$$M_x \tilde{M}_y = \{\overline{E}|100\}\tilde{M}_y M_x = -e^{ik_x}\tilde{M}_y M_x. \quad (23)$$

And on X-M, $k_x = \pi/L_x$, so we have commutation relation $[M_x, \tilde{M}_y] = 0$. One notes that for a state $|u\rangle$ with M_x eigenvalue g_x, its Kramers partner $\tilde{M}_y T |u\rangle$ satisfies

$$M_x(\tilde{M}_y T |u\rangle) = -g_x(\tilde{M}_y T |u\rangle). \quad (24)$$

This shows that $|u\rangle$ and $\tilde{M}_y T |u\rangle$ have opposite eigenvalue g_x. Therefore, for each k point on X-M, there must be a twofold-degenerate doublet $\{|u\rangle, \tilde{M}_y T |u\rangle\}$.

Next, we turn to the dispersion on path Γ-X: $(k_x, 0, 0)$. Since Γ-X lies on $k_y = 0$ plane, which is invariant under $\tilde{M}_y$, thus each Bloch state $|u\rangle$ there can be chosen as an eigenstate of $\tilde{M}_y$. Moreover, we have

$$\tilde{M}_y^2 = \{\overline{E}|100\} = -e^{ik_x}, \quad (25)$$

hence its eigenvalue g_y must be $\pm i e^{i\frac{k_x}{2}}$. Additionally, Γ and X are both at time reversal invariant momenta, which are invariant under T. Specifically, $g_y = \pm i$ at Γ, each Kramers pair $|u\rangle$ and $T |u\rangle$ must have opposite eigenvalue g_y. At the same time, $g_y = \pm 1$ at X$(\pi/L_x, 0, 0)$, thus each Kramers pair

$|u\rangle$ and $T |u\rangle$ must have the same g_y. Therefore, there must be a partner-switching when going from Γ to X, leading to an hourglass-type dispersion, as schematically illustrated in Fig. 2(f). It has to mention that the crossing point of the hourglass is a twofold-degenerate Weyl point, and is robust due to it is formed by two orthogonal mirror branches. A similar analysis also applies to the hourglass fermion on Y-M.

So far, our analysis uncovers the existence of twofold-degenerate Weyl nodal line and hourglass fermions, which are both protected by nonsymmorphic space group symmetries. In following, we will show that above symmetry analysis is also completely consistent with our numerical calculation results.

2. Numerical result

From symmetry perspective, the inversion symmetry P would vanish and thus original space group changes, which strongly affect the degeneracy and band crossings in the band structure. The band structure for Lattice1 with the addition of Rashba SOC is shown in Fig. 2(d) and several new features can be observed: (i) Original Dirac nodal line along X-M splits into two twofold-degenerate nodal lines (Weyl nodal line). (ii) There emerge hourglass-type dispersions on Γ-X and Y-M [see Fig. 2(e) for a 3D image], respectively. These numerical results are also highly consistent with aforementioned symmetry analysis.

In this section, we have revealed some exotic band-crossings protected by nonsymmorphic symmetries in Lattice1 under patterned 2DEG frame. On one hand, when intrinsic SOC considered alone, there exists a Dirac nodal line. On the other hand, when Rashba SOC also added, there emerge two Weyl nodal lines and two hourglass points, as summarized in Table I. A very similar analysis for Lattice2 are given in the following section.

IV. LATTICE2

A. $\lambda \neq 0$, $\alpha = 0$: two Dirac nodal lines

1. Symmetry analysis

We first give a detailed symmetry analysis on possible nontrivial band crossings for Lattice2 in intrinsic SOC case.

When intrinsic SOC present, the lattice structure of Lattice2 belongs to space group $Pbam$ (No. 55) and there are three generators: inversion P, twofold rotation C_{2z} and screw-axis rotation $\{C_{2y}|\frac{1}{2}\frac{1}{2}0\}$. By combining these three operations, we can obtain other two glide mirrors $\tilde{M}_x : (x, y, z) \rightarrow (-x + \frac{1}{2}, y + \frac{1}{2}, z)$ and $\tilde{M}_y : (x, y, z) \rightarrow (x + \frac{1}{2}, -y + \frac{1}{2}, z)$. In addition, time reversal symmetry T is also preserved.

It is noted that path X-M is an invariant subspace of M_z, $\tilde{M}_y T$ and $\tilde{M}_x$. Similar to the analysis in Lattice1 case, one finds that $(\tilde{M}_y T)^2 = -1$ on X-M, hence it requires a Kramer-like double degeneracy for each k point on X-M. Moreover, since M_z is anticommutative with $\tilde{M}_x$, thus the degeneracy further doubles into fourfold, leading to a Dirac nodal line on X-M path in the end. Similar analysis also applies to the Dirac nodal line on path Y-M.

2. Numerical result

Similar to previous discussion in Lattice1, we then perform band structure calculation in the presence of intrinsic SOC for
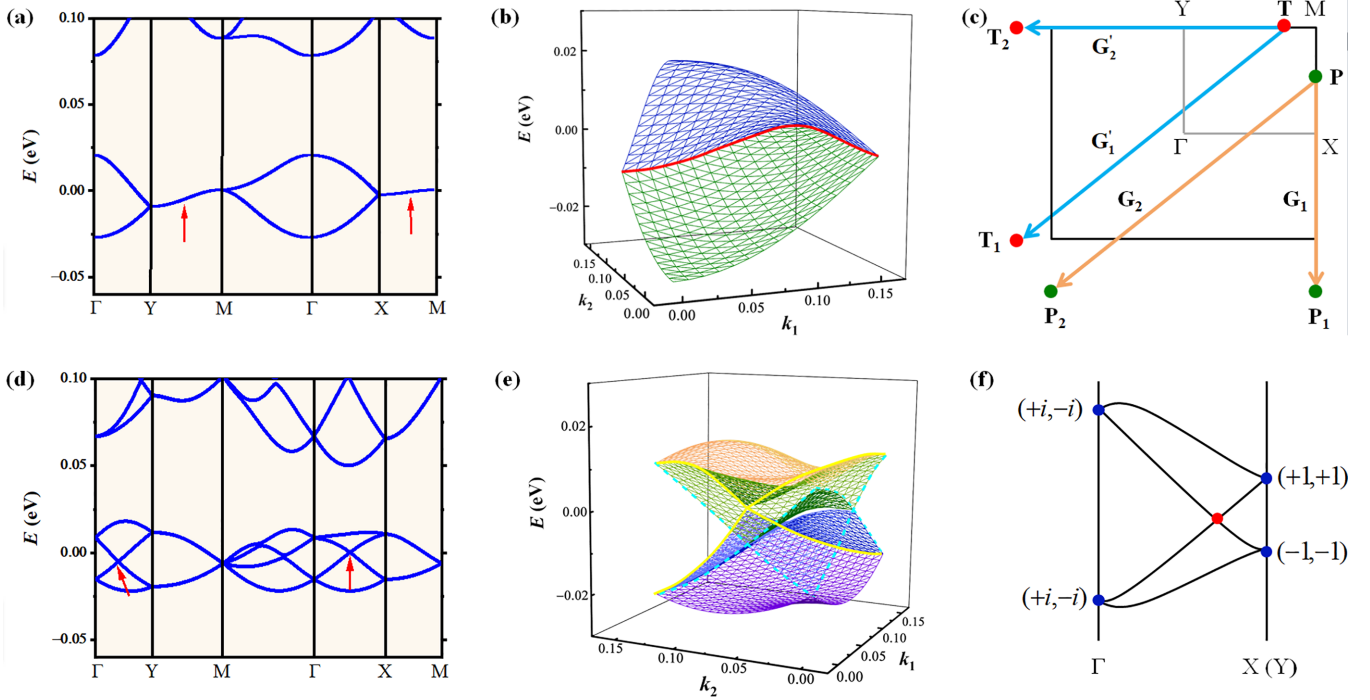
FIG. 3. Calculated band structures for the lowest four bands in presence of intrinsic SOC and Rashba SOC for Lattice2. Band structure along high-symmetry paths in (a) intrinsic SOC case and in (d) both intrinsic SOC and Rashba SOC case. The 3D plot in (b) shows two 1D Dirac nodal lines, indicated by a red solid line, along BZ boundary in intrinsic SOC case and that in (e) shows two hourglass-type dispersions and four Weyl nodal lines, indicated with cyan dashed lines and yellow solid lines, respectively, in both intrinsic SOC and Rashba SOC case. (c) Illustration of translation for $\mathbf{P}(\mathbf{T})$ on Dirac nodal line to $\mathbf{P}_1(\mathbf{T}_1)$ and $\mathbf{P}_2(\mathbf{T}_2)$. The orange and blue lines represent translations for points on nodal line X-M and Y-M, respectively. (f) Schematic figure shows the hourglass dispersion along path Γ-X (Γ-Y), characterized by a hourglass cone with four degenerate points at boundary (blue dot) and one degenerate point at center (red dot). The numbers in the bracket denote the eigenvalue g_y/g_x at the degenerate point. In our calculation, $U_0 = 0.3$ eV, $L_x = 20$ nm, $L_y = 25$ nm, $m^* = 0.02 m_e$, $d = 10$ nm, $\lambda = 7.2 \times 10^{-18}$ m^2, $\alpha = 3 \times 10^{-10}$ eV m. The degenerate point energy at M in (a) and between Γ-X in (d) is set to zero, respectively.

Lattice2. As shown in Fig. 3(a), in this case, we observe degenerate and almost flat bands (Dirac nodal lines, see Fig. 3(b) for a more clear 3D plot) along BZ boundary X-M and Y-M, respectively. Obviously, the band structure results also highly agree with our symmetry analysis above.

3. k · p approximation

Herein we derive analytical solution for Lattice2 [Fig. 3(c)]. On one hand, according Eq. (20) in Sec. III A, we can immediately write the dispersion relation for nodal line M-X:

$$E(\mathbf{q}) = \frac{\hbar^2}{2m^*}\left\{ \mathbf{q}^2 \pm \frac{2\pi}{L_x}q_x + 2\left(k_y - \frac{2\pi}{L_y}\right)q_y + \frac{\pi^2}{L_x^2} \right.$$
$$\left. + \left(k_y - \frac{2\pi}{L_y}\right)^2 \right\} + V_0, \qquad (26)$$

where $V_0 = \frac{\pi d^2 U_0}{2A}$. On the other hand, for nodal line M-Y, we mainly concentrate on the states with wave vector $\mathbf{q}' + \mathbf{T}$ near arbitrary $\mathbf{T}$ point on M-Y, i.e., $|\mathbf{q}'| \ll \mathbf{T}$, where $\mathbf{T} = (k_x, \pi/L_y, 0)$, $k_x \in (-\pi/L_x, \pi/L_x)$. Analogy to Eq. (15), the wave function $\psi_{\mathbf{k}}(\mathbf{r})$ then can be expanded into a similar form as

$$\psi_{\mathbf{k}}(\mathbf{r}) = \frac{1}{\sqrt{2A}}[c_1' e^{i(\mathbf{k}+\mathbf{G}_1')\cdot\mathbf{r}} + c_2' e^{i(\mathbf{k}+\mathbf{G}_2')\cdot\mathbf{r}}]. \qquad (27)$$

Let us substitute $\mathbf{k}$ for $\mathbf{q}' + \mathbf{T}$, thus $\psi_{\mathbf{k}}(\mathbf{r})$ can further be expressed as

$$\psi_{\mathbf{q}}'(\mathbf{r}) = \frac{1}{\sqrt{2A}}[c_1' e^{i(\mathbf{q}'+\mathbf{T}_1)\cdot\mathbf{r}} + c_2' e^{i(\mathbf{q}'+\mathbf{T}_2)\cdot\mathbf{r}}], \qquad (28)$$

in which the basis $(\mathbf{T}_1, \mathbf{T}_2)$ also have a same energy for pure 2DEG and are connected by the minimum reciprocal vector $\mathbf{G}_1'/\mathbf{G}_2'$ with $\mathbf{T}$. Within this basis, the Hamiltonian in Eq. (3) would be written into

$$H(\mathbf{q}') = \begin{bmatrix} \frac{\hbar^2}{2m^*}(\mathbf{q}'+\mathbf{T}_1)^2 + V_0 & V_{1'-2'} \\ V_{2'-1'} & \frac{\hbar^2}{2m^*}(\mathbf{q}'+\mathbf{T}_2)^2 + V_0 \end{bmatrix}, \qquad (29)$$

in which the antidiagonal term also can be obtained using Eq. (2):

$$V_{1'-2'} = V_{2'-1'}^* = \frac{\pi d U_0 J_1\left(\frac{1}{2}|\mathbf{G}_{1-2}'|d\right)}{A|\mathbf{G}_{1-2}'|}\{1 + e^{-i\cdot 2\pi\cdot\delta_1}$$
$$+ e^{-i\cdot\pi} + e^{-i\cdot 2\pi\left(\frac{1}{2}+\delta_1\right)}\} = 0. \qquad (30)$$

Therefore Hamiltonian Eq. (29) changes into

$$H(\mathbf{q}') = \begin{bmatrix} \frac{\hbar^2}{2m^*}(\mathbf{q}'+\mathbf{T}_1)^2 + V_0 & 0 \\ 0 & \frac{\hbar^2}{2m^*}(\mathbf{q}'+\mathbf{T}_2)^2 + V_0 \end{bmatrix}. \qquad (31)$$

By solving the eigenvalues of above matrix, we obtain the analytical solution of energy dispersion for nodal line M-Y very easily:

$$E(\mathbf{q}') = \frac{\hbar^2}{2m^*}\left\{\mathbf{q}'^2 + 2\left(k_x - \frac{2\pi}{L_x}\right)q'_x \pm \frac{2\pi}{L_y}q'_y\right.$$
$$\left. + \left(k_x - \frac{2\pi}{L_x}\right)^2 + \frac{\pi^2}{L_y^2}\right\} + \frac{\pi d^2 U_0}{A}. \quad (32)$$

Obviously, the analytical solution results also hold true for the nodal line in Lattice3, but require replacing L_x/L_y with L (see Appendix A).

B. $\lambda \neq 0$, $\alpha \neq 0$: two hourglass Weyl points

1. Symmetry analysis

In this section, we give a detailed symmetry analysis on possible nontrivial band crossings when both intrinsic SOC and Rashba SOC are considered simultaneously for Lattice2.

Similarly, once Rashba SOC involved, original space group *Pbam* (No. 55) is reduced to *Pba*2 (No. 32). Now the generators are two glide mirrors: $\tilde{M}_x : (x, y, z) \rightarrow (-x + \frac{1}{2}, y + \frac{1}{2}, z)$ and $\tilde{M}_y : (x, y, z) \rightarrow (x + \frac{1}{2}, -y + \frac{1}{2}, z)$. In the following text, we show that there are four twofold-degenerate Weyl nodal lines and two hourglass Weyl points, also resulted from nonsymmorphic symmetries.

Firstly, we concentrate on nontrivial topological states on X-M and Y-M, which can be argued in a similar way as before: briefly, path X-M is invariant under the anti-unitary symmetry $\tilde{M}_yT$, and it is important to note that $(\tilde{M}_yT)^2 = -1$ still holds in presence of Rashba SOC. This guarantees a Kramer-like double degeneracy on X-M. A similar analysis also can be found on Y-M.

Secondly, the dispersion on Γ-X and Γ-Y can be understood as following: Note that every k point on Γ-X is invariant under $\tilde{M}_y$, so each Bloch state $|u\rangle$ can be chosen as an eigenstate of $\tilde{M}_y$. Since

$$\tilde{M}_y^2 = \{\overline{E}|100\} = -e^{ik_x}, \quad (33)$$

which is the same as Eq. (25), thus there certainly still exists an hourglass fermion. As for Γ-Y, every k point on it is invariant under $\tilde{M}_x$. Since

$$\tilde{M}_x^2 = \{\overline{E}|010\} = -e^{ik_y}, \quad (34)$$

thus its eigenvalue g_x must be $\pm ie^{i\frac{k_y}{2}}$. Additionally, Γ and Y are at time reversal invariant momenta, which are invariant under T. At Γ, $g_x = \pm i$, each Kramers pair $|u\rangle$ and $T|u\rangle$ must have opposite eigenvalue g_x. At the same time, at point $Y(0, \pi/L_y, 0)$, $g_x = \pm 1$, each Kramers pair $|u\rangle$ and $T|u\rangle$ must have the same g_x. Therefore, there must be another partner-switching when going from Γ to Y, leading to another hourglass-type dispersion, as schematically illustrated in Fig. 3(f).

Finally we turn to k point M, which is invariant under the symmetry $\tilde{M}_x$, $\tilde{M}_y$, and T. Remarkably, we note that for a state $|u\rangle$ with $\tilde{M}_x$ eigenvalue g_x at M, its Kramers partner $T|u\rangle$ must have the same eigenvalue g_x (because $g_x = \pm 1$). Meanwhile, we have

$$M_x(\tilde{M}_y|u\rangle) = -g_x(\tilde{M}_y|u\rangle), \quad (35)$$
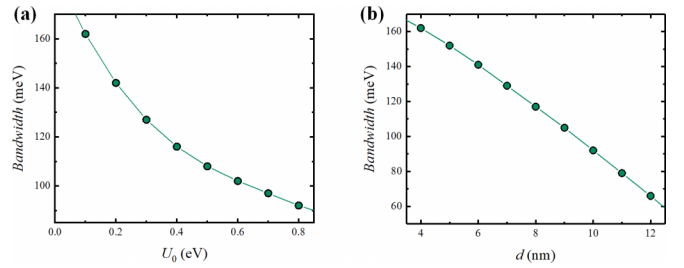
showing the two orthogonal states $|u\rangle$ and $\tilde{M}_y|u\rangle$ have opposite g_x. Therefore, the four states $\{u, T|u\rangle, \tilde{M}_y|u\rangle, \tilde{M}_yT|u\rangle\}$ are linearly independent and degenerate with the same energy, that is to say, a 4D irreducible representation shows up, which results in a fourfold-degenerate Dirac fermion at the M point.

2. Numerical result

The band structure in Rashba SOC case is shown in Figs. 3(d)–3(e), and we can observe the following three features: (i) The bands along X-M and Y-M split into two doublets (corresponding to original Dirac nodal lines in absence of Rashba SOC); (ii) Two hourglass Weyl points appear at Γ-X and Γ-Y, respectively; (iii) A 2D Dirac point appears at M point, which is fourfold-degenerate and has linear dispersion. Obviously, these results also highly agree with above symmetry analysis.

In this section, we have revealed some exotic band crossings protected by nonsymmorphic symmetries in Lattice2 under patterned 2DEG frame. On one hand, when intrinsic SOC considered alone, there exist two Dirac nodal lines. On the other hand, when Rashba SOC also added, there emerge four Weyl nodal lines and two hourglass points, as summarized in Table I. A very similar analysis for Lattice3 are also given in Appendix A.

V. PARAMETER EFFECT

In order to explore the effect of potential value U_0 and diameter d on bandwidth of the lowest bands that we concerned, which can be directly detected by angle resolved photoemission spectroscopy in experiment, we carry out relevant calculations, and the results (taking Lattice1 for example) are displayed in Fig. 4. Clearly, the bandwidth will reduce when U_0 or d increases, and it even almost depends antilinearly on d. Figure 5 shows the band structures for Lattice1 with different parameters (effective mass m^*, lattice constant $L/(L_x, L_y)$ and potential value U_0), and we can observe the following four features: (i) As U_0 increased, linear dispersive energy window is dramatically broadened; (ii) The group velocity at Dirac point remains constant as U_0 increased; (iii) As m^* or L increased, a significant reduction of the bandwidth can be found; (iv) A smaller U_0 leads to a bigger bandwidth.
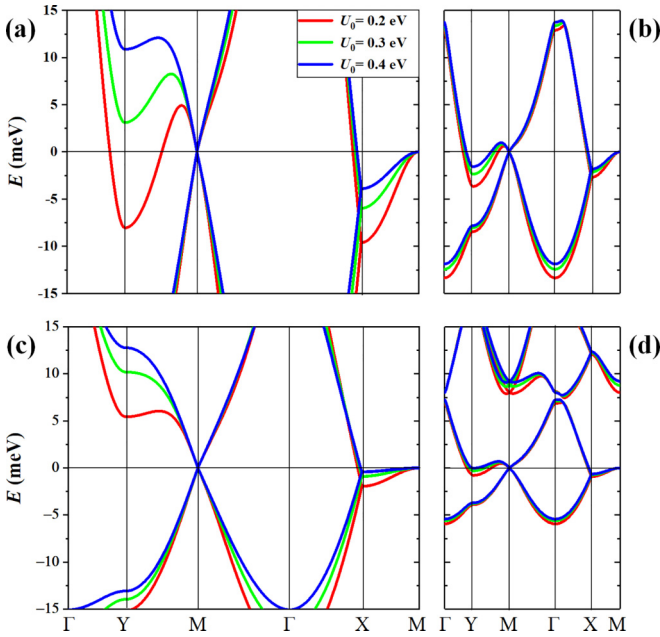
FIG. 5. Calculated band structures of the lowest bands for Lattice1 with (a) $m^* = 0.02m_e$, $L = 20$ nm. (b) $m^* = 0.02m_e$, $L = 40$ nm. (c) $m^* = 0.04m_e$, $L = 20$ nm. (d) $m^* = 0.04m_e$, $L = 40$ nm. In our calculation, $d = 10$ nm, $\lambda = 3.2 \times 10^{-18}$ m^2, and the energy of the crossing point at M is set to zero for clarity.

VI. DISCUSSION AND CONCLUSION

It is crucial that such nontrivial band crossings to be close to the Fermi level for manifestation of interesting physics, which can be achieved by doping or other mechanisms in practice. For example, the charge density required to dope the system to reach the nodal lines and hourglass Weyl points energy is $3 \sim 4 \times 10^{11}$ cm^{-2}, which is in the range of typical value in 2DEG studies [82], and may be tuned by applying a gate voltage or by light illumination [83]. Some particular advantages of our system include: (i) The nodal lines have quite small energy change in BZ; (ii) The patterned 2DEG model is relatively easy to realize in experiment. Moreover, the hourglass-type dispersion was previously confirmed in ex-

periment as surface states of 3D topological insulators KHgX (X=As, Sb, Bi) [37]. The possibility of hourglass-type dispersion in 3D bulk systems was also studied in half-metal Mg$_2$VO$_4$ [63] and models [62], whereas, the energy range of hourglass-type dispersion in these examples is especially small. In comparison, the energy window and splitting degree of hourglass-type dispersion proposed here can be extremely large by tuning relevant parameters.

What is more, we also consider the effect of an out-of-plane magnetic field on the hourglass fermions in our system, which can be realized by adding an Zeeman term on the original Hamiltonian. As shown in Fig. 6, we find that the hourglass Weyl points are gapped both in Lattice1 and Lattice2 (the results for Lattice3 see Appendix A). We also note that the two fold-degenerate nodal line on X-M or Y-M (only for Lattice2) does not split, the reason is that $\tilde{M}_y T$ or $\tilde{M}_x T$ symmetry is still preserved.

In conclusion, we have shown numerically and theoretically that multiple types of band crossings appear when an appropriate nanometer-scale period potential patterned with nonsymmorphic symmetries is applied to a conventional 2DEG model. We find that in presence of intrinsic SOC, our systems host 1D Dirac nodal lines. Further, with the introduction of Rashba SOC, then the original Dirac nodal lines split and there appear hourglass fermions. Prominently, all the band crossings are entirely determined by extrinsic nonsymmorphic symmetries, therefore they are quite robust. Moreover, the energy dispersion perpendicular to each nodal line is linear, and both the group velocity and bandwidth can be easily tuned by external parameters such as effective mass and lattice constant. In addition, we expect that some exotic phenomena would be discovered in our system, such as novel anisotropic electrodynamics [84], large spin Hall conductivity [85,86], giant magnetoresistance [87,88] and anisotropic transport of electrons. Our system indeed has provide a promising platform for investigating varieties of topological phases and phase transitions. At present, crystal face controlling [37] and surface alloy [38,39] are two methods to create wallpaper groups, here in this work, patterned 2DEG provides an additional method to engineer wallpaper groups. It is expected that our system can be fabricated and the predictions proposed here can also be readily verified in the near future.
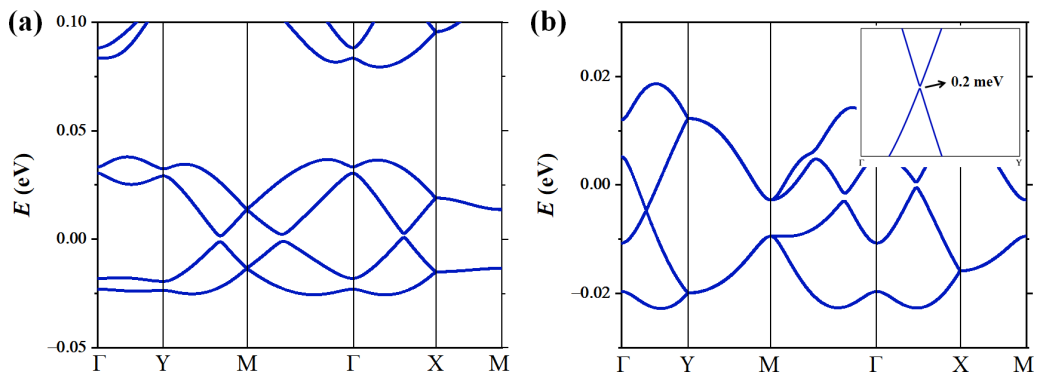
FIG. 6. Band structures for Lattice1 and Lattice2 with a Zeeman term along the z direction. (a) $U_0 = 0.8$ eV, $L_x = 20$ nm, $L_y = 25$ nm, $m^* = 0.02m_e$, $d = 10$ nm, $\lambda = 3.2 \times 10^{-18}$ m^2, $\alpha = 3 \times 10^{-10}$ eV m. The value of the Zeeman term energy is taken to be 2.9×10^{-3} eV. (b) $U_0 = 0.3$ eV, $L_x = 20$ nm, $L_y = 25$ nm, $m^* = 0.02m_e$, $d = 10$ nm, $\lambda = 7.2 \times 10^{-18}$ m^2, $\alpha = 3 \times 10^{-10}$ eV m. The value of the Zeeman term energy is taken to be 4.6×10^{-3} eV. The inset in (b) gives a magnified band structure along Γ-Y, showing a very small gap about 0.2 meV.

APPENDIX A: LATTICE3

In Secs. III and IV, we have uncovered underlying nontrivial band crossings for Lattice1 and Lattice2 both in intrinsic SOC and Rashba SOC case. Here we present detailed analysis for Lattice3 in both cases.

1. $\lambda \neq 0$, $\alpha = 0$: one Dirac nodal line

a. Symmetry analysis

First of all, when only intrinsic SOC considered, Lattice3 belongs to space group $P4/mbm$ (No. 127), and there are three generators: inversion P, fourfold rotation C_{4z}, and screw-axis rotation $\{C_{2x}|\frac{1}{2}\frac{1}{2}0\}$. By combining the above three operations, we can further get two glide mirrors $\tilde{M}_x : (x, y, z) \rightarrow (-x + \frac{1}{2}, y + \frac{1}{2}, z)$ and $\tilde{M}_y : (x, y, z) \rightarrow (x + \frac{1}{2}, -y + \frac{1}{2}, z)$. Similarly, time reversal symmetry T is still preserved.

The X-M path is an invariant subspace of M_z, so each Bloch state $|u\rangle$ on the path can be chosen as an eigenstate of M_z. One finds that on X-M,

$$M_z^2 = \overline{E} = -1, \tag{A1}$$

hence the eigenvalues of M_z along this path are $g_z = \pm i$.

We note that each k point on X-M is also invariant under the combined antiunitary operation $\tilde{M}_y T$. Since

$$(\tilde{M}_y T)^2 = e^{ik_x} = -1 \tag{A2}$$

on X-M, thus the bands along it have a Kramer-like double degeneracy. Moreover, the commutation relation between M_z and $\tilde{M}_y$ on X-M is

$$M_z \tilde{M}_y = \overline{E} \tilde{M}_y M_z, \tag{A3}$$

i.e., anticommutation relation $\{M_z, \tilde{M}_y\} = 0$. Hence, for an eigenstate $|u\rangle$ with M_z eigenvalue g_z, we have

$$M_z(\tilde{M}_y T |u\rangle) = g_z(\tilde{M}_y T |u\rangle), \tag{A4}$$

indicating the two Kramers partners $|u\rangle$ and $\tilde{M}_y T |u\rangle$ share same eigenvalue g_z.

Additionally, X-M is also the invariant subspace of $\tilde{M}_x$. The commutation relation between M_z and $\tilde{M}_x$ is

$$M_z \tilde{M}_x = \overline{E} \tilde{M}_x M_z, \tag{A5}$$

namely, $\{M_z, \tilde{M}_x\} = 0$ on X-M, thus again we have

$$M_z(\tilde{M}_x |u\rangle) = -g_z(\tilde{M}_x |u\rangle). \tag{A6}$$

In total, we get four degenerate orthogonal states: $\{|u\rangle, \tilde{M}_y T |u\rangle, \tilde{M}_x |u\rangle, (\tilde{M}_y T)\tilde{M}_x |u\rangle\}$, forming a Dirac nodal line on X-M.

b. Numerical results

The band structures in presence of intrinsic SOC are shown in Figs. 7(a)–7(b), and we can observe very similar band features like Lattice2: (i) each band is at least twofold-degenerate due to PT symmetry; (ii) the bands along X-M path form a fourfold-degenerate Dirac nodal line, and the dispersion along it is quite flat. Apparently, the band results validate above symmetry analysis.

c. $\mathbf{k} \cdot \mathbf{p}$ approximation

Herein we derive the solution for Dirac nodal line on X-M in Lattice3.

Let us consider the nodal lines in Lattice3 (Fig. 7). According to Eq. (20) in Sec. III, we can immediately write the dispersion relation for nodal line M-X:

$$E(\mathbf{q}) = \frac{\hbar^2}{2m^*} \left\{ \mathbf{q}^2 \pm \frac{2\pi}{L}q_x + 2\left(k_y - \frac{2\pi}{L}\right)q_y + \frac{\pi^2}{L^2} \right.$$
$$\left. + \left(k_y - \frac{2\pi}{L}\right)^2 \right\} + V_0, \tag{A7}$$

where $V_0 = \frac{\pi d^2 U_0}{2A}$.

2. $\lambda \neq 0$, $\alpha \neq 0$: one hourglass Weyl point

a. Symmetry analysis

When Rashba SOC involved, Lattice3 belongs to space group $P4bm$ (No. 100), in this case, there are two generators: fourfold rotation C_{4z} and glide mirror $\tilde{M}_y : (x, y, z) \rightarrow (x + \frac{1}{2}, -y + \frac{1}{2}, z)$. Combining these two operations, we can obtain another glide mirror $\tilde{M}_x : (x, y, z) \rightarrow (-x + \frac{1}{2}, y + \frac{1}{2}, z)$.

We first consider the topological states on X-M $(\pi/L_x, k_y, 0)$, where $-\pi/L_y < k_y \leqslant \pi/L_y$. The path is invariant under $\tilde{M}_x$, so each Bloch state $|u\rangle$ can be chosen as an eigenstate of $\tilde{M}_x$. We have

$$\tilde{M}_x^2 = \{\overline{E}|010\} = -e^{ik_y} \tag{A8}$$

on X-M, hence the eigenvalue g_x of $\tilde{M}_x$ must be $\pm i e^{ik_y/2}$.

Note that each k point on X-M is also invariant under the combined antiunitary operation $\tilde{M}_y T$. Since

$$(\tilde{M}_y T)^2 = e^{ik_x} = -1 \tag{A9}$$

on X-M, therefore the bands along this path will have a Kramer-like double degeneracy. Moreover, the commutation relation between $\tilde{M}_x$ and $\tilde{M}_y$ is

$$\tilde{M}_x \tilde{M}_y = \{\overline{E}|\bar{1}10\}\tilde{M}_y \tilde{M}_x = e^{ik_y}\tilde{M}_y \tilde{M}_x. \tag{A10}$$

Therefore we find that for a state $|u\rangle$ with $\tilde{M}_x$ eigenvalue g_x, its Kramers partner $\tilde{M}_y T |u\rangle$ would satisfy

$$\tilde{M}_x(\tilde{M}_y T |u\rangle) = -g_x(\tilde{M}_y T |u\rangle), \tag{A11}$$

showing that $|u\rangle$ and $\tilde{M}_y T |u\rangle$ have opposite eigenvalue. Therefore, there must be a twofold-degenerate doublet $\{|u\rangle, \tilde{M}_y T |u\rangle\}$ for each k point on X-M.
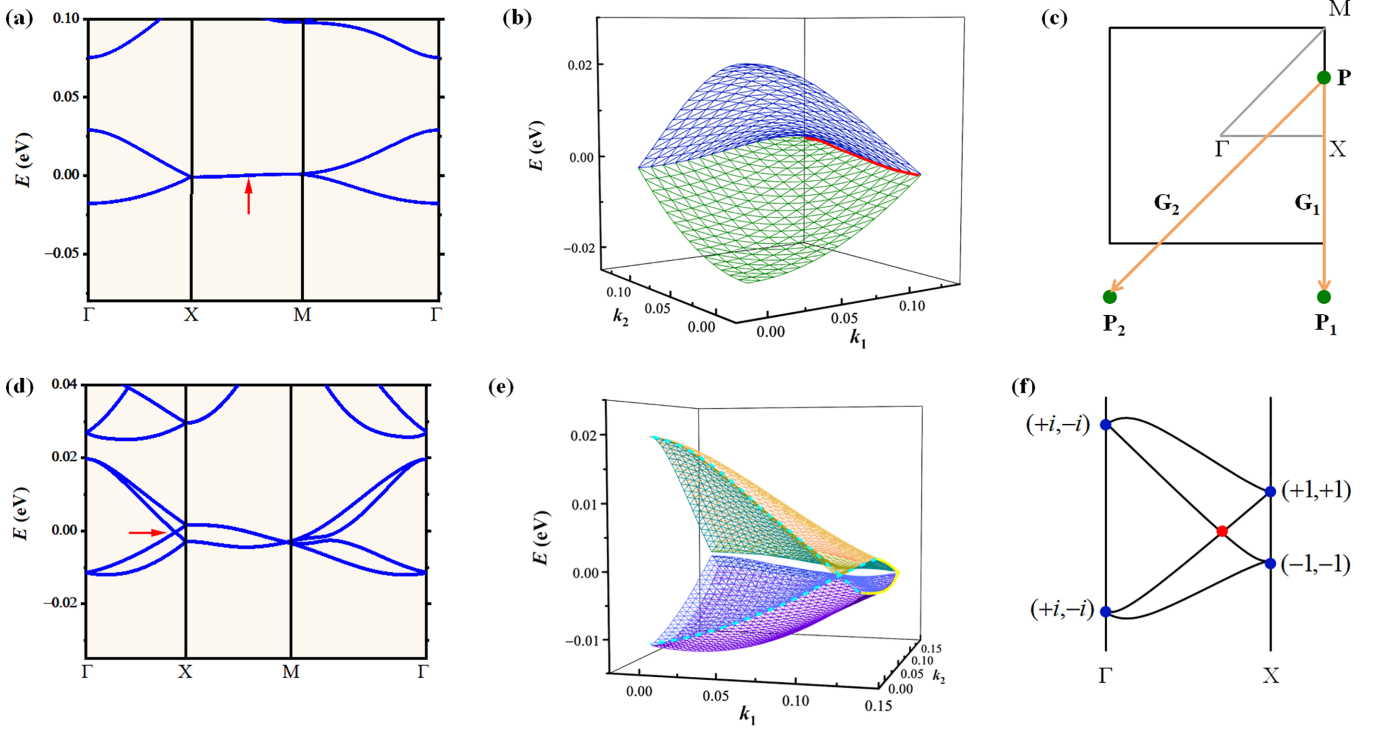
FIG. 7. Calculated band structures of the lowest four bands in presence of intrinsic SOC and Rashba SOC for Lattice3. Band structures along high-symmetry paths in (a) intrinsic case and in (d) both intrinsic SOC and Rashba SOC case. The 3D plot in (b) shows a 1D Dirac nodal line, indicated by a red solid line, along X-M in intrinsic SOC case and that in (e) shows an hourglass-type dispersion and two Weyl nodal lines, indicated with cyan dashed lines and yellow solid lines, respectively, in both intrinsic SOC and Rashba SOC case. (c) Illustration of the translation for **P** on Dirac nodal line X-M to $\mathbf{P}_1$ and $\mathbf{P}_2$. (f) A same hourglass dispersion as in previous two lattices. In our calculation, $U_0 = 0.3$ eV, $L = 25$ nm, $m^* = 0.02 \ m_e$, $d = 10$ nm, $\lambda = 7.2 \times e^{-18}$ m^2, $\alpha = 8 \times e^{-10}$ eV m. The degenerate point energy at M in (a) and between Γ-X in (d) is set to zero, respectively.

Next, we turn to the band dispersion on path Γ-X $(k_x, 0, 0)$. Since the path lies on $k_y = 0$ plane, which is invariant under $\tilde{M}_y$, so each Bloch state $|u\rangle$ on Γ-X can be chosen as an eigenstate of $\tilde{M}_y$. We have

$$\tilde{M}_y^2 = \{\overline{E}|100\} = -e^{ik_x}, \tag{A12}$$
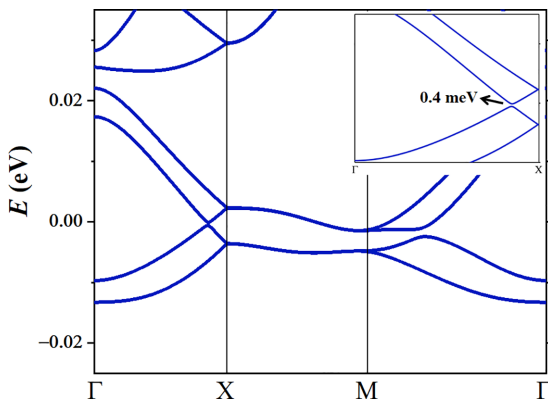
FIG. 8. Band structure with a Zeeman term along the z direction for Lattice3. In our calculation, $U_0 = 0.3$ eV, $L = 23$ nm, $m^* = 0.02 m_e$, $d = 10$ nm, $\lambda = 7.2 \times 10^{-18}$ m^2, $\alpha = 8 \times 10^{-10}$ eV m. The value of the Zeeman term energy is taken to be 4.6×10^{-3} eV. The inset gives a magnified band structure along Γ-X, showing a very small gap about 0.4 meV.

hence, its eigenvalue g_y must be $\pm i e^{ik_x/2}$. Additionally, Γ and X are both time reversal invariant momenta, thus we can infer that: At Γ, $g_y = \pm i$, each Kramers pair $|u\rangle$ and $T |u\rangle$ must have opposite eigenvalue, and at X, $g_y = \pm 1$, each Kramers pair $|u\rangle$ and $T |u\rangle$ must have same eigenvalue. On the whole, there must be a partner-switching when going from Γ to X, leading to an hourglass-type dispersion, as schematically illustrated in Fig. 7(f).

b. Numerical results

The band structures for Lattice3 in Rashba SOC case are shown in Figs. 7(d)–7(e). Similar features can be observed: (i) The Dirac nodal line along X-M is gapped and then splits into two twofold-degenerate Weyl nodal lines; (ii) There emerges an hourglass fermion between Γ and X, which validate our symmetry analysis again.

APPENDIX B: BAND STRUCTURE WITH OUT-OF-PLANE MAGNETIC FIELD

In the main text, we have discussed the band structures with out-of-plane magnetic field for Lattice1 and Lattice2. Here, the result for Lattice3 are shown in Fig. 8.

[1] M. Z. Hasan and C. L. Kane, Rev. Mod. Phys. **82**, 3045 (2010).

[2] B. A. Bernevig, T. L. Hughes, and S. C. Zhang, Science **314**, 1757 (2006).

[3] C. X. Liu, T. L. Hughes, X. L. Qi, K. Wang, and S. C. Zhang, Phys. Rev. Lett. **100**, 236601 (2008).

[4] D. Hsieh, D. Qian, L. Wray, Y. Xia, Y. S. Hor, R. J. Cava, and M. Z. Hasan, Nature (London) **452**, 970 (2008).

[5] H. Zhang, C. X. Liu, X. L. Qi, X. Dai, Z. Fang, and S. C. Zhang, Nat. Phys. **5**, 438 (2009).

[6] N. P. Armitage, E. J. Mele, and A. Vishwanath, Rev. Mod. Phys. **90**, 015001 (2018).

[7] Y. Du, F. Tang, D. Wang, L. Sheng, E. J. Kan, C. G. Duan, S. Y. Savrasov, and X. G. Wan, npj Quantum Mater. **2**, 3 (2017).

[8] K. N. Zhang, M. Z. Yan, H. X. Zhang, H. Q. Huang, M. Arita, Z. Sun, W. H. Duan, Y. Wu, and S. Y. Zhou, Phys. Rev. B **96**, 125102 (2017).

[9] J. F. Khoury, A. J. E. Rettie, M. A. Khan, N. J. Ghimire, I. Robredo, J. E. Pfluger, K. Pal, C. Wolverton, A. Bergara, J. S. Jiang, L. M. Schoop, M. G. Vergniory, J. F. Mitchell, D. Y. Chung, and M. G. Kanatzidis, J. Am. Chem. Soc. **141**, 19130 (2019).

[10] A. Bafekry, C. Stampfl, M. Faraji, M. Yagmurcukardes, M. M. Fadlallah, H. R. Jappor, M. Ghergherehchi, and S. A. H. Feghhi, Appl. Phys. Lett. **118**, 203103 (2021).

[11] T. R. Chang, S. Y. Xu, D. S. Sanchez, W. F. Tsai, S. M. Huang, G. Q. Chang, C. H. Hsu, G. Bian, I. Belopolski, Z. M. Yu, S. A. Yang, T. Neupert, H. T. Jeng, H. Lin, and M. Z. Hasan, Phys. Rev. Lett. **119**, 026404 (2017).

[12] D. F. Liu, J. Liang, E. K. Liu, Q. N. Xu, Y. W. Li, C. Chen, D. Pei, W. J. Shi, S. K. Mo, P. Dudin, T. Kim, C. Cacho, G. Li, Y. Sun, L. X. Yang, Z. K. Liu, S. S. P. Parkin, C. Felser, and Y. L. Chen, Science **365**, 1282 (2019).

[13] P. Puphal, V. Pomjakushin, N. Kanazawa, V. Ukleev, D. J. Gawryluk, J. Ma, M. Naamneh, N. C. Plumb, L. Keller, R. Cubitt, E. Pomjakushina, and J. S. White, Phys. Rev. Lett. **124**, 017202 (2020).

[14] H. Yang, Y. Sun, Y. Zhang, W. J. Shi, S. S. P. Parkin, and B. H. Yan, New J. Phys. **19**, 015008 (2017).

[15] X. P. Li, K. Deng, B. T. Fu, Y. K. Li, D. S. Ma, J. F. Han, J. H. Zhou, S. Y. Zhou, and Y. G. Yao, Phys. Rev. B **103**, L081402 (2021).

[16] J. Jiang, Z. Liu, Y. Sun, H. F. Yang, C. R. Rajamathi, Y. P. Qi, L. X. Yang, C. Chen, H. Peng, C.-C. Hwang, S. Z. Sun, S.-K. Mo, I. Vobornik, J. Fujii, S. S. P. Parkin, C. Felser, B. H. Yan, and Y. L. Chen, Nat. Commun. **8**, 13973 (2017).

[17] M. Y. Yao, N. Xu, Q. S. Wu, G. Autes, N. Kumar, V. N. Strocov, N. C. Plumb, M. Radovic, O. V. Yazyev, C. Felser, J. Mesot, and M. Shi, Phys. Rev. Lett. **122**, 176402 (2019).

[18] Q. N. Xu, R. Yu, Z. Fang, X. Dai, and H. M. Weng, Phys. Rev. B **95**, 045136 (2017).

[19] J. He, X. Kong, W. Wang, and S. P. Kou, New J. Phys. **20**, 053019 (2018).

[20] Y. Wang, Y. T. Qian, M. Yang, H. X. Chen, C. Li, Z. Y. Tan, Y. Q. Cai, W. J. Zhao, S. Y. Gao, Y. Feng, S. Kumar, E. F. Schwier, L. Zhao, H. M. Weng, Y. G. Shi, G. Wang, Y. T. Song, Y. B. Huang, K. Shimada, Z. Y. Xu *et al.* Phys. Rev. B **103**, 125131 (2021).

[21] M. M. Hosen, K. Dimitri, I. Belopolski, P. Maldonado, R. Sankar, N. Dhakal, G. Dhakal, T. Cole, P. M. Oppeneer, D. Kaczorowski, F. C. Chou, M. Z. Hasan, T. Durakiewicz, and M. Neupane, Phys. Rev. B **95**, 161101(R) (2017).

[22] Z. H. Li, W. Wang, P. Zhou, Z. S. Ma, and L. Z. Sun, New J. Phys. **21**, 033018 (2019).

[23] X. B. Wang, X. M. Ma, E. Emmanouilidou, B. Shen, C. H. Hsu, C. S. Zhou, Y. Zuo, R. R. Song, S. Y. Xu, G. Wang, L. Huang, N. Ni, and C. Liu, Phys. Rev. B **96**, 161112(R) (2017).

[24] Z. J. Wang, B. J. Wieder, J. Li, B. H. Yan, and B. A. Bernevig, Phys. Rev. Lett. **123**, 186401 (2019).

[25] Z. Liu, H. D. Wang, Z. F. Wang, J. L. Yang, and F. Liu, Phys. Rev. B **97**, 155138 (2018).

[26] L. L. An, X. D. Zhu, W. S. Gao, M. Wu, W. Ning, and M. L. Tian, Phys. Rev. B **99**, 045143 (2019).

[27] C. Mondal, C. K. Barman, S. Kumar, A. Alam, and B. Pathak, Sci. Rep. **9**, 527 (2019).

[28] T. L. He, X. M. Zhang, Y. Liu, X. F. Dai, L. Y. Wang, and G. D. Liu, Phys. Rev. B **104**, 045143 (2021).

[29] M. R. Khan, K. Bu, and J. T. Wang, New J. Phys. **24**, 043007 (2022).

[30] E. Cheng, W. Xia, X. Shi, Z. H. Yu, L. Wang, L. M. Yan, D. C. Peets, C. C. Zhu, H. Su, Y. Zhang, D. Z. Dai, X. Wang, Z. Q. Zou, N. Yu, X. F. Kou, W. G. Yang, W. W. Zhao, Y. F. Guo, and S. Y. Li, npj Quantum Mater. **5**, 38 (2020).

[31] A. Lau, T. Hyart, C. Autieri, A. Chen, and D. I. Pikulin, Phys. Rev. X **11**, 031017 (2021).

[32] X. P. Li, B. T. Fu, D. S. Ma, C. X. Cui, Z. M. Yu, and Y. G. Yao, Phys. Rev. B **103**, L161109 (2021).

[33] R. A. Molina and J. Gonzalez, Phys. Rev. Lett. **120**, 146601 (2018).

[34] W. B. Rui, Y. X. Zhao, and A. P. Schnyder, Phys. Rev. B **97**, 161113(R) (2018).

[35] T. Matsushita, S. Fujimoto, and A. P. Schnyder, Phys. Rev. Res. **2**, 043311 (2020).

[36] D. Sinha and A. Taraphder, Phys. Rev. B **104**, 245141 (2021).

[37] J. Z. Ma, C. J. Yi, B. Q. Lv, Z. J. Wang, S. M. Nie, L. Wang, L. Y. Kong, Y. B. Huang, P. Richard, P. Zhang, K. Yaji, K. Kuroda, S. Shin, H. M. Weng, B. A. Bernevig, Y. G. Shi, T. Qian, and H. Ding, Sci. Adv. **3**, e1602415 (2017).

[38] Z. F. Wang, B. Liu, and W. Zhu, Phys. Rev. Lett. **123**, 126403 (2019).

[39] M. Y. Tian, J. F. Wang, X. F. Liu, W. W. Chen, Z. Liu, H. J. Du, X. C. Ma, X. F. Cui, A. D. Zhao, Q. W. Shi, Z. F. Wang, Y. Luo, J. L. Yang, B. Wang, and J. G. Hou, Nano Lett. **20**, 2157 (2020).

[40] G. L. Cheng, M. Tomczyk, S. C. Lu, J. P. Veazey, M. C. Huang, P. Irvin, S. Ryu, H. Lee, C. B. Eom, C. S. Hellberg, and J. Levy, Nature (London) **521**, 196 (2015).

[41] Z. L. Li, T. Cao, M. Wu, and S. G. Louie, Nano Lett. **17**, 2280 (2017).

[42] T. S. Gardenier, J. J. V. D. Broeke, J. R. Moes, I. Swart, C. Delerue, M. R. Slot, C. M. Smith, and D. Vanmaekelbergh, ACS Nano **14**, 13638 (2020).

[43] S. S. Yue, H. Zhou, D. Y. Geng, Z. Y. Sun, M. Arita, K. Shimada, P. Cheng, L. Chen, S. Meng, K. H. Wu, and B. J. Feng, Phys. Rev. B **102**, 201401(R) (2020).

[44] S. Wang, D. Scarabelli, L. Du, Y. Y. Kuznetsova, L. N. Pfeiffer, K. W. West, G. C. Gardner, M. J. Manfra, V. Pellegrini, S. J. Wind, and A. Pinczuk, Nat. Nanotechnol. **13**, 29 (2018).

[45] C. H. Park and S. G. Louie, Nano Lett. **9**, 1793 (2009).

[46] Z. R. Liu, J. Y. Wang, and J. L. Li, Phys. Chem. Chem. Phys. **15**, 18855 (2013).

[47] S. Li, W. X. Qiu, and J. H. Gao, Nanoscale **8**, 12747 (2016).

[48] C. P. García, V. Pellegrini, A. Pinczuk, M. Rontani, G. Goldoni, E. Molinari, B. S. Dennis, L. N. Pfeiffer, and K. W. West, Phys. Rev. Lett. **95**, 266806 (2005).

[49] M. Gibertini, A. Singha, V. Pellegrini, M. Polini, G. Vignale, A. Pinczuk, L. N. Pfeiffer, and K. W. West, Phys. Rev. B **79**, 241406(R) (2009).

[50] W. Pan, S. K. Lyo, J. L. Reno, J. A. Simmons, D. Li, and S. R. J. Brueck, Appl. Phys. Lett. **92**, 052104 (2008).

[51] K. K. Gomes, W. Mar, W. Ko, F. Guinea, and H. C. Manoharan, Nature (London) **483**, 306 (2012).

[52] S. Wang, L. Z. Tan, W. Wang, S. G. Louie, and N. Lin, Phys. Rev. Lett. **113**, 196803 (2014).

[53] M. Zhou, Z. Liu, W. M. Ming, Z. F. Wang, and F. Liu, Phys. Rev. Lett. **113**, 236802 (2014).

[54] J. Lobo-Checa, M. Matena, K. Müller, J. H. Dil, F. Meier, L. H. Gade, T. A. Jung, and M. Stöhr, Science **325**, 300 (2009).

[55] S. Wang, W. Wang, L. Z. Tan, X. G. Li, Z. Shi, G. Kuang, P. N. Liu, S. G. Louie, and N. Lin, Phys. Rev. B **88**, 245430 (2013).

[56] C. Cen, S. Thiel, J. Mannhart, and J. Levy, Science **323**, 1026 (2009).

[57] B. S. Jessen, L. Gammelgaard, M. R. Thomsen, D. M. A. Mackenzie, J. D. Thomsen, J. M. Caridad, E. Duegaard, K. Watanabe, T. Taniguchi, T. J. Booth, T. G. Pedersen, A. P. Jauho, and P. Bøggild, Nat. Nanotechnol. **14**, 340 (2019).

[58] S. Zhao, Z. Li, and J. Yang, J. Am. Chem. Soc. **136**, 13313 (2014).

[59] T. Sato, Z. W. Wang, K. Nakayama, S. Souma, D. Takane, Y. Nakata, H. Iwasawa, C. Cacho, T. Kim, T. Takahashi, and Y. Ando, Phys. Rev. B **98**, 121111(R) (2018).

[60] H. Wu, A. M. Hallas, X. Cai, J. W. Huang, J. S. Oh, V. Loganathan, A. Weiland, G. T. McCandless, J. Y. Chan, S. K. Mo, D. H. Lu, M. Hashimoto, J. Denlinger, R. J. Birgeneau, A. H. Nevidomskyy, G. Li, E. Morosan, and M. Yi, npj Quantum Mater. **7**, 31 (2022).

[61] S. Li, Y. Liu, S. S. Wang, Z. M. Yu, S. Guan, X. L. Sheng, Y. G. Yao, and S. A. Yang, Phys. Rev. B **97**, 045131 (2018).

[62] L. Y. Wang, S. K. Jian, and H. Yao, Phys. Rev. B **96**, 075110 (2017).

[63] H. P. Zhang, X. M. Zhang, T. L. He, X. F. Dai, Y. Liu, G. D. Liu, L. Y. Wang, and Y. Zhang, Phys. Rev. B **102**, 155116 (2020).

[64] S. S. Wang, Y. Liu, Z. M. Yu, X. L. Sheng, and S. A. Yang, Nat. Commun. **8**, 1844 (2017).

[65] R. W. Zhang, Z. Y. Zhang, C. C. Liu, and Y. G. Yao, Phys. Rev. Lett. **124**, 016402 (2020).

[66] P.-Y. Chang, O. Erten, and P. Coleman, Nat. Phys. **13**, 794 (2017).

[67] R.-X. Zhang, F. Wu, and S. Das Sarma, Phys. Rev. Lett. **124**, 136407 (2020).

[68] B. Feng, B. Fu, S. Kasamatsu, S. Ito, P. Cheng, C. C. Liu, Y. Feng, S. Wu, S. K. Mahatha, P. Sheverdyaeva, P. Moras, M. Arita, O. Sugino, T. C. Chiang, K. Shimada, K. Miyamoto, T. Okuda, K. Wu, L. Chen, Y. Yao *et al.*, Nat. Commun. **8**, 1007 (2017).

[69] M. Cameau, R. Yukawa, C. H. Chen, A. Huang, S. Ito, R. Ishibiki, K. Horiba, Y. Obata, T. Kondo, H. Kumigashira, H. T. Jeng, M. D'angelo, and I. Matsuda, Phys. Rev. Mater. **3**, 044004 (2019).

[70] S. Roth, G. Gatti, A. Crepaldi, and M. Grioni, Electron. Struct. **1**, 014001 (2019).

[71] L. Gao, J.-T. Sun, J.-C. Lu, H. Li, K. Qian, S. Zhang, Y.-Y. Zhang, T. Qian, H. Ding, X. Lin, S. X. Du, and H. J. Gao, Adv. Mater. **30**, 1707055 (2018).

[72] Z. Wang, A. Alexandradinata, R. J. Cava, and B. A. Bernevig, Nature (London) **532**, 189 (2016).

[73] B. J. Wieder, B. Bradlyn, Z. J. Wang, J. Cano, Y. Kim, H.-S. D. Kim, X. M. Rappe, C. L. Kane, and B. A. Bernevig, Science **361**, 246 (2018).

[74] C.-X. Liu, R.-X. Zhang, and B. K. VanLeeuwen, Phys. Rev. B **90**, 085304 (2014).

[75] K. Shiozaki, M. Sato, and K. Gomi, Phys. Rev. B **91**, 155120 (2015).

[76] C. Fang and L. Fu, Phys. Rev. B **91**, 161105(R) (2015).

[77] B.-J. Yang, T. A. Bojesen, T. Morimoto, and A. Furusaki, Phys. Rev. B **95**, 075135 (2017).

[78] Y. H. Liu, Y. Z. Wang, N. C. Hu, J. Y. Lin, C. H. Lee, and X. Zhang, Phys. Rev. B **102**, 035142 (2020).

[79] D.-C. Ryu, J. Kim, H. Choi, and B. I. Min, J. Am. Chem. Soc. **142**, 19278 (2020).

[80] N. W. Ashcroft and N. D. Mermin, *Solid State Physics* (Saunders College Publishing, Fort Worth, TX, 1976).

[81] P. Y. Yu and M. Cardona, *Fundamentals of Semiconductors: Physics and Materials Properties* (Springer, New York, 2001).

[82] J. T. Devreese and F. M. Peeters, *The Physics of the Two-Dimensional Electron Gas* (Plenum, New York, 1987).

[83] C. Albrecht, J. H. Smet, D. Weiss, K. von Klitzing, R. Hennig, M. Langenbuch, M. Suhrke, U. Rössler, V. Umansky, and H. Schweizer, Phys. Rev. Lett. **83**, 2234 (1999).

[84] Y. M. Shao, Z. Y. Sun, Y. Wang, C. C. Xu, R. Sankar, A. J. Breindel, C. Cao, M. M. Fogler, F. C. Chou, Z. Q. Li, T. Timusk, M. B. Maple, and D. N. Basov, Proc. Natl. Acad. Sci. USA **116**, 1168 (2019).

[85] W. Hou, J. Liu, X. Zuo, J. Xu, X. Y. Zhang, D. S. Liu, M. W. Zhao, Z. G. Zhu, H. G. Luo, and W. S. Zhao, npj Comput. Mater. **7**, 37 (2021).

[86] Y. Sun, Y. Zhang, C. X. Liu, C. Felser, and B. H. Yan, Phys. Rev. B **95**, 235104 (2017).

[87] J. Yang, Z. Y. Song, L. Guo, H. Gao, Z. Dong, Q. Yu, R. K. Zheng, T. T. Kang, and K. Zhang, Nano Lett. **21**, 10139 (2021).

[88] E. Emmanouilidou, B. Shen, X. Y. Deng, T. R. Chang, A. S. Shi, G. Kotliar, S. Y. Xu, and N. Ni, Phys. Rev. B **95**, 245113 (2017).